

Additive Manufacturing of Powdery Ni-Based Superalloys Mar-M-247 and CM 247 LC in Hybrid Laser Metal Deposition



ANDRÉ SEIDEL, THOMAS FINASKE, ARIANE STRAUBEL, HORST WENDROCK,
TIM MAIWALD, MIRKO RIEDE, ELENA LOPEZ, FRANK BRUECKNER,
and CHRISTOPH LEYENS

The present paper addresses the phenomena of hot cracking of nickel-based superalloys in the perspective of hybrid Laser Metal Deposition (combined application of induction and laser). This includes an extract of relevant theoretical considerations and the deduction of the tailored approach which interlinks material–scientific aspects with state-of-the-art manufacturing engineering. The experimental part reflects the entire process chain covering the manufacturing strategy, important process parameters, the profound analysis of the used materials, the gradual process development, and the corresponding hybrid manufacture of parts. Furthermore, hot isostatic pressing and thermal treatment are addressed as well as tensile testing at elevated temperatures. Further investigations include X-ray CT measurements, electron backscattered diffraction (EBSD), and scanning electron microscopy (SEM) as well as light optical microscope evaluation. The fundamental results prove the reliable processibility of the high-performance alloys Mar-M-247 and Alloy 247 LC and describe in detail the process inherent microstructure. This includes the grain size and orientation as well as the investigation of size, shape, and distribution of the γ' precipitates and carbides. Based on these findings, the manufacturing of more complex demonstrator parts with representative dimensions is addressed as well. This includes the selection of a typical application, the transfer of the strategy, as well as the proof of concept.

<https://doi.org/10.1007/s11661-018-4777-y>

© The Minerals, Metals & Materials Society and ASM International 2018

I. INTRODUCTION AND MOTIVATION

LASER metal deposition (LMD) is a state-of-the-art additive manufacturing process and regarded as one of the key technologies in the future of production engineering. LMD is classified as a direct energy deposition process in which high-concentrated energy is used to bond the filler material and the substrate material by

means of strongly localized heat input resulting in a distinctive narrow heat-affected zone (HAZ) (see Figure 1). After solidification, the deposited material is generally characterized by metallurgical bonding with low dilution between the weld bead and the layer below, and an almost complete avoidance of porosity.

The process development for high-temperature materials is an important area of research. These materials demonstrate unique properties like excellent resistance to mechanical and chemical degradations under thermal exposure.^[1] Typical applications of these alloys are in aerospace and marine industries, nuclear reactors, and industrial gas turbines. One example is the Ni-based superalloy *Mar-M-247*. The alloy was developed in the early 1970s by the *Martin Marietta Corporation* and contains eleven elements beside the base element nickel.^[2] Gunderson *et al.* evaluated *Mar-M-247* as one of the most difficult alloys to be processed by conventional fusion welding.^[3] In fact, there is a distinct tendency to hot cracking. These cracks are linked to the interval between the liquidus and solidus temperatures and occur as intercrystalline and/or interdendritic cracks. After their local occurrence, a distinction is

ANDRÉ SEIDEL, TIM MAIWALD, and CHRISTOPH LEYENS are with the Fraunhofer-Institute for Material and Beam Technology, Winterbergstraße 28, 01277 Dresden, Germany and also with the Technische Universität Dresden, Helmholtzstr. 7, 01069 Dresden, Germany. Contact e-mail: andre.seidel@iws.fraunhofer.de THOMAS FINASKE, MIRKO RIEDE, and ELENA LOPEZ are with the Fraunhofer-Institute for Material and Beam Technology. ARIANE STRAUBEL is with the Technische Universität Dresden. HORST WENDROCK is with the Leibniz-Institut für Festkörper- und Werkstofforschung Dresden, Helmholtzstr. 20, 01069 Dresden, Germany. FRANK BRUECKNER is with the Fraunhofer-Institute for Material and Beam Technology and also with the Luleå University of Technology, 971 87 Luleå, Sweden.

Manuscript submitted March 13, 2018.

Article published online July 5, 2018

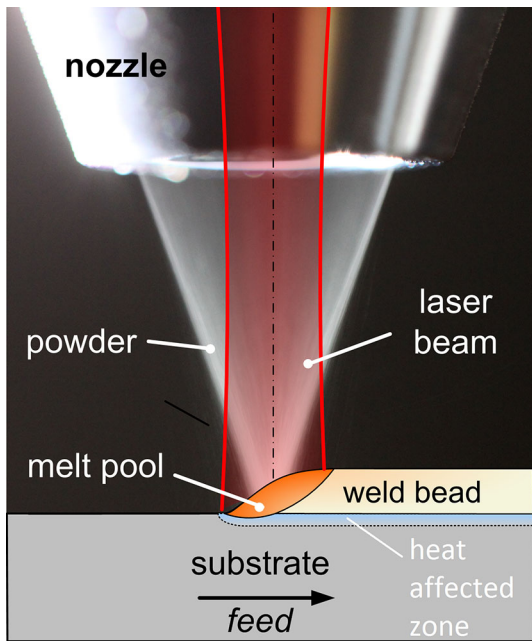


Fig. 1—Schematic illustration of the Laser Metal Deposition process zone with presentation of the powder cone, the laser, the melt pool, the weld bead, the heat-affected zone, and the substrate material (Color figure online).

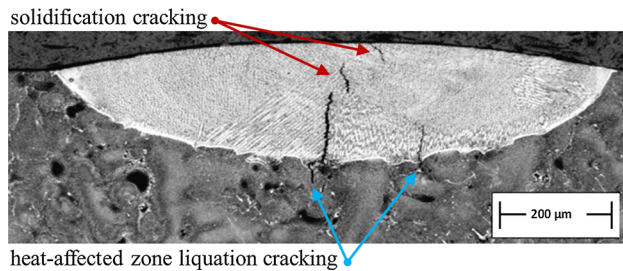


Fig. 2—Light microscopy image of a cross section showing solidification cracking and heat-affected zone liquation cracking of a single weld bead manufactured *via* LMD by means of Mar-M-247 powder material and a Mar-M-247 ingot substrate material.

made between solidification cracking and heat-affected zone liquation cracking (see Figure 2).

There exist a variety of strategies currently used to avoid hot cracking, such as metallurgical methods like the adjustments of the base material,^[4] the filler material,^[5] the process gas,^[6] the adjustment of the melt pool dimensions,^[7] the superimposition of compressive stresses,^[8] temperature control adjustment,^[9] or their combination in terms of thermomechanical control,^[10–12] as well as magnetofluid dynamic methods.^[13] However, the modifications of the alloy composition for the filler and/or the base material and the application of active gas instead of inert gas are often rather ruled out as an option from the point of view of practical applications. In contrast, applicable and viable concepts for the prevention of hot cracking can be found in the field of hybrid machining. The latter hybrid-machining approaches are defined as controlled interaction of process mechanisms and/or energy sources frequently applied for achieving a

significant improvement of process performance.^[14,15] In this study, defect-free processing is investigated *via* appropriate energy source coupling by combining laser radiation with induction heating.

A. Laser-Induced Melt Pool, Solidification, and the Phenomena of Hot Cracking

The applied laser beams have a Gaussian intensity distribution whereby the induced melt pools show a maximum temperature in the center decreasing toward solidification temperature at the phase boundaries (see Figure 3). As a consequence, there is observed a temperature-induced gradient of the surface tension at the liquid–gas interface.^[16,17] Latter is the predominant driving force of the Marangoni convection. According to Wu, the value of flow velocity is in the magnitude of 10 to 100 cm/s.^[18] Brueckner notes that the interaction is limited to the region in the proximity to the liquid-gas interface.^[12]

However, since the solidification process on the micro-scale level determines the mechanical properties,^[19] a differentiated assessment shall be addressed in the following. Based on the temporally and strongly localized heat input with very little HAZ, there is a rapid solidification. Considering the moving laser beam, there are position-dependent temperature gradient G and growth rate R along the melt pool (see Figure 4(a)). Starting with a planar solidification at the fusion line the morphology changes to cellular, columnar dendritic and equiaxed dendritic.

The thermal gradient is initially positive, and the direction of the heat flow points from the inner melt pool toward the lower-temperature substrate. The result is a solidification front which is initially planar (see Figure 4) with a bulk composition which complies with the nominal composition C_0 . Subsequently, there is a change of the local thermal state due to the feed of the laser, heat conduction into the substrate material, as well as convection and heat radiation at the solid–gas interface. The thermal gradient changes from positive to negative, and the planar solidification front becomes destabilized.^[21] The melt in front of the solid/liquid interface is undercooled by primary undercooling from the temperature gradient,

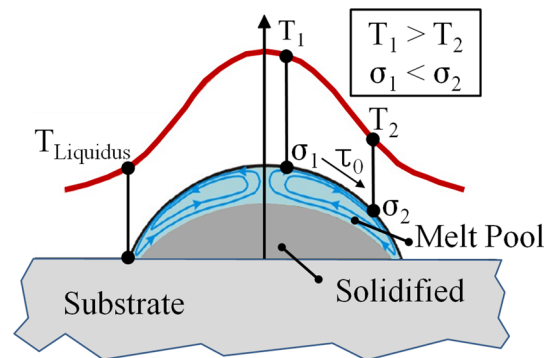


Fig. 3—Temperature-induced gradient of the surface tension and the resulting Marangoni convection with qualitative presentation of the temperature T , the surface tension Φ , and the shear stress τ . Reprinted with permission from Ref. [12] (Color figure online).

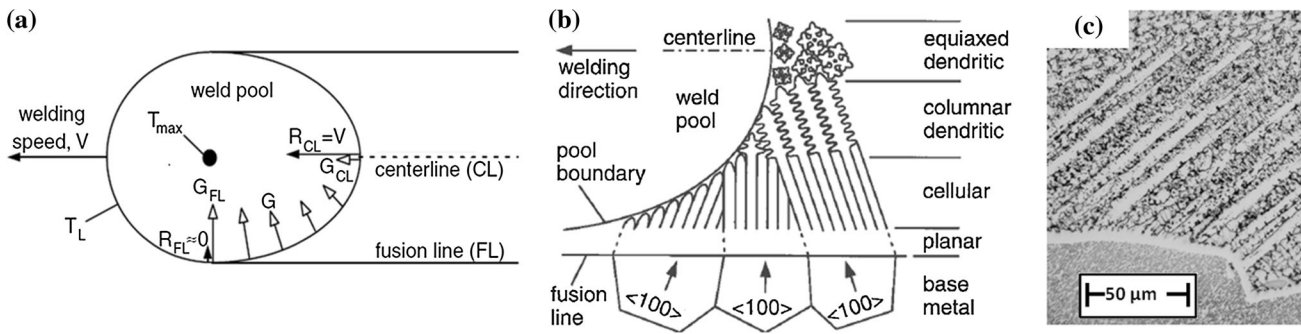


Fig. 4—(a) Variations in temperature gradient G and growth rate R along the weld pool boundary, adapted from Ref. [20]. (b) Variation in solidification morphology across the fusion zone, reprinted with permission from Ref. [20]. (c) Corresponding experimental results from the LMD with powder of Mar-M-247 on a Mar-M-247 ingot material without application of additional heat sources.

Table I. Composition of the Alloys Studied in Weight Percent (Ni-Base)

	Ni	Co	W	Cr	Al	Ta	Hf	Ti	Mo	C	Zr	B
Mar-M-247	bal.	10.0	10.0	8.25	5.5	3.0	1.5	1.0	0.7	0.15	0.05	0.015
CM 247 LC	bal.	9.2	9.5	8.1	5.6	3.2	1.4	0.7	0.5	0.07	0.015	0.015
$k^{[23-26]}$		> 1	≥ 1	> 1	< 1	≪ 1	< 1	< 1	< 1	—	—	—

followed by an increasing curvature undercooling because of the change of the solid/liquid interface, and finally by constitutional undercooling driven from the solutal field of the alloy.^[19] The ratio between the solid composition and the liquid composition at the interface changes depending on the particular equilibrium partition coefficient k of the alloying elements. The elements are distributed homogeneously for $k = 1$, preferably in the dendrites for $k > 1$, and in the dendritic spacing and/or the grain boundaries for $k < 1$.^[22] The value of the partition coefficient k varies for each particular element depending on nominal composition of the alloy.^[22] The corresponding table (see Table I) shows the chemical composition for the superalloys Mar-M-247 and CM 247 LC according to Gunderson *et al.*^[2] as well as an estimation for the partition coefficient k according to References 23 through 26.

The melting temperature of the remaining melt within the interdendritic spacing is often significantly lower.^[3] The interdendritic spacing is generally considered as a starting point of crack initiation. Various theories such as the shrinkage brittleness theory,^[27] the strain theory,^[28,29] and the generalized theory^[30] have been proposed as scientific description of the interaction between the existing mechanical and metallurgical factors. Rappaz *et al.* describe the nonplanar solidification front with associated shrinkage of the bulk where the shrinkage and strain can frequently be compensated by interdendritic liquid feeding. In this way, the dendritic network is able to develop some mechanical resistance to tensile stresses through coherency.^[31] If the shrinkage stresses cannot be compensated by interdendritic liquid feeding and/or coherency, localized strain may initiate hot cracking. Hence, there is the need to carefully control the induced strain and/or ensure interdendritic liquid feeding.

B. Thermally Induced Stresses, Process Monitoring and Control, Manufacturing Strategy

In the current study, the suppression of solidification cracking and heat-affected zone liquation cracking was achieved *via* the development and application of tailored temperature cycles. This was realized by energy source coupling (induction and laser) in combination with appropriate process monitoring and control equipment.^[32] Thereby, the temperature gradient between the melt pool and the substrate material was substantially reduced. Hence, gradients in thermal expansion and or thermally induced stresses can be controlled effectively by precise thermal tailoring (Figure 5).

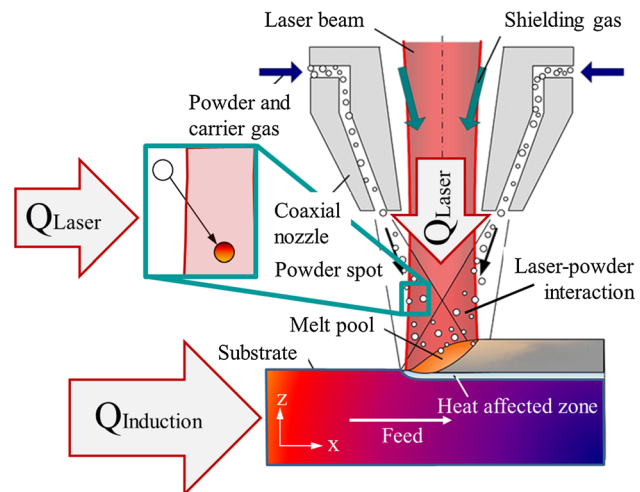


Fig. 5—Illustration of the laser metal deposition process zone with the schematic illustration of the laser–powder interaction and the energy input *via* inductive heating, Adapted with permission from Ref. [12] (Color figure online).

This was achieved by the application of a camera-based sensor system named »E-MAqS«, which is an acronym for Emission Matrix Acquiring System.^[32] In this system, an industrial gray scale CCD camera is used with sufficient sensitivity in the near infrared. With a melting range significantly above temperatures of 700 °C, the signal is high enough to get thermal images with adequate accuracy.^[32] The visible light and the

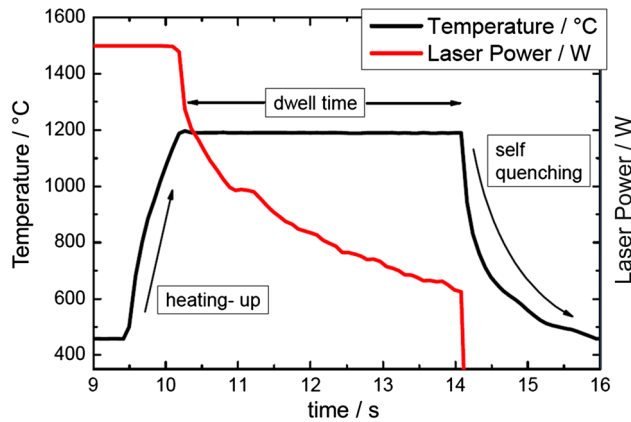


Fig. 6—Schematic illustration of the process data of a temperature-controlled laser material processing, while the temperature was measured using a pyrometer MAURER KTR 1075. Reprinted with permission from Ref. [32].

laser light are cut off from the incoming radiation with special filters. The camera generates an image at a single wavelength of 740 nm. Hence, all gray scale values can be assigned to local temperatures at a laser-irradiated surface. Calibration was done with a standard black body radiator. The nonlinear correlation between temperature and gray scale value is taken into account by the software of »E-MAqS«. The temperature range can be adjusted by changing parameters like exposure, attenuation, and aperture. Applying »E-MAqS« as a coaxially adapted system, the specific attenuation of the laser optics must be taken into account. The thermal image is analyzed by the software. A variety of different features and algorithms are able to deliver selected localized information on the thermal balance of the process. As a consequence, a steady-state condition can be assured during the additive material build-up avoiding the accumulation of heat (Figure 6).

II. RESULTS AND DISCUSSIONS

A. Constituent Materials

A Mar-M-247 ingot was used as substrate material. The ingot was processed *via* vacuum melting and consists of rather coarse grains with a dendritic structure (see Figures 7(a) and (b)). A further

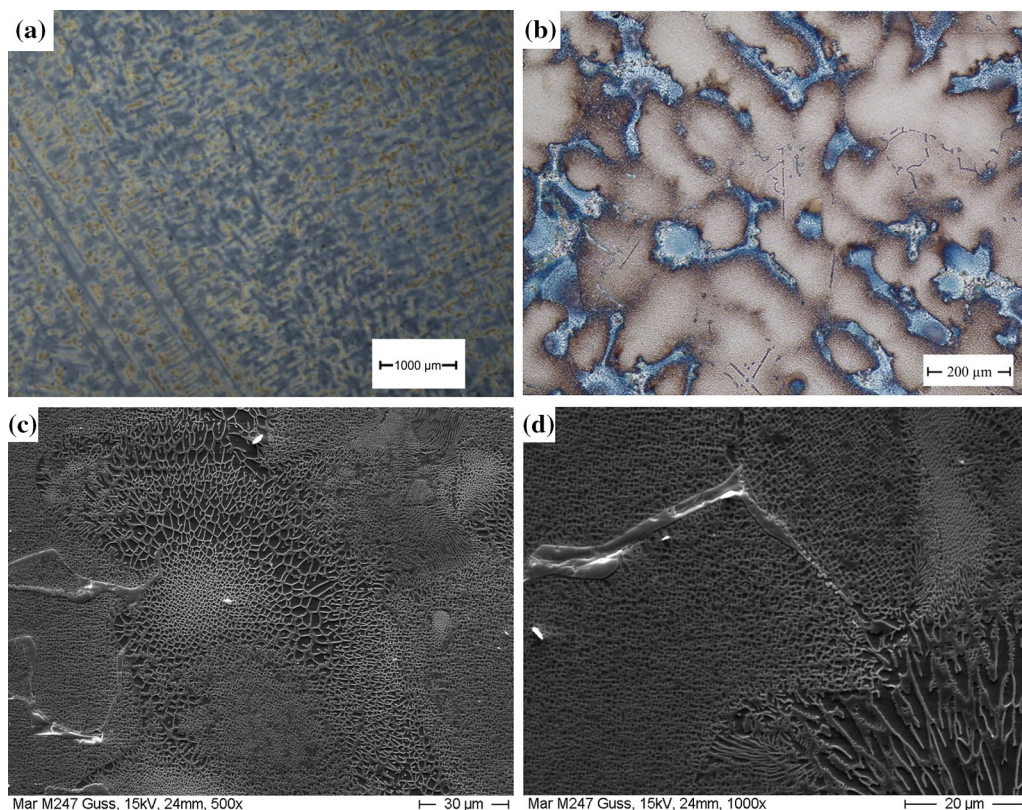


Fig. 7—(a) Light microscopy image of a cross section showing the microstructure of Mar-M-247 ingot material in the as-cast condition with dendrites (fawn) and interdendritic spacing (blue). (b) Magnified section from the interdendritic area of the ingot material with dendrites (fawn) and interdendritic spacing (blue). The samples were etched with 200 mL H₂O, 50 mL HCL, 50 mL HNO₃, 0.5 g MoO₃. (c and d) Scanning electron microscopy images of an interdendritic region of the Mar-M-247 as-cast ingot material showing the multiphase microstructure with the γ' precipitates of Ni₃ (Al,Ti,Ta) (dark) in the γ -matrix (gray) and strip-type carbides (light-gray) (Color figure online).

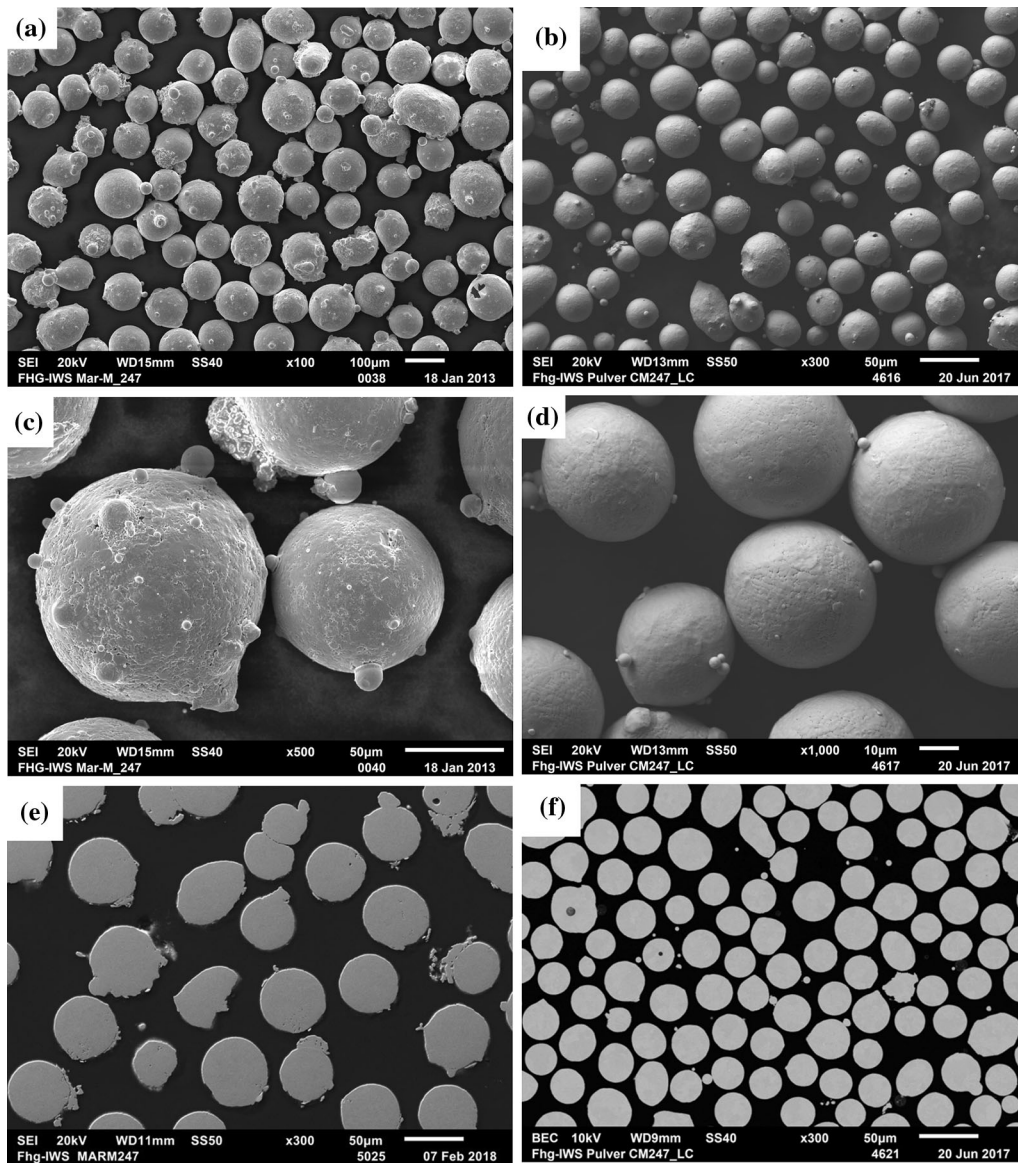


Fig. 8—(a) Gas-atomized (argon) Mar-M-247 powder. (b) Gas-atomized (argon) CM 247 LC powder. (c) Representative Mar-M-247 powder particles showing a rough surface texture and sporadic satellite formation. (d) Representative CM 247 LC powder particles with a smooth surface and isolated satellite formation. (e) SEM images of metallographic sections of the powder material for the evaluation of the density for Mar-M-247. (f) SEM images of metallographic sections of CM 247 LC.

magnification of the interdendritic areas of the ingot material can be seen in c and d. One can see the multiphase microstructure with the γ' precipitates of $\text{Ni}_3(\text{Al,Ti,Ta})$ (black) in the γ -matrix (gray) and strip-type carbides. Furthermore, it is evident that the size and shape of the γ' precipitates are rather inhomogeneous in the as-cast condition.

Furthermore, gas-atomized (argon) spherical powder material was used as filler material for the laser metal deposition process (see Figure 5). Both materials show a microdendritic surface texture and sporadic or isolated satellite formation. In the following, the powder particle density was investigated *via* metallographic sections. It can be seen that the particles are rather dense with isolated micropores with an expansion in the range of a

few microns (see Figures 8(e) and (f)). This applies to Mar-M-247 and CM 247 LC in the same manner.

Laser diffraction was used to determine the particle size distribution (PSD). The PSD of the Mar-M-247 powder is within the size range of 45 to 80 μm (Figure 9(a)). The D0.1, D0.5, and D0.9 refer to the maximum sizes corresponding to 10, 50, or 90 pct of the particles. The Mar-M-247 powder shows a lognormal distribution with D0.5 at 69.8 μm and a span of 0.614. The PSD of the CM 247 LC powder is within the size range of 25 to 45 μm (Figure 9(b)). The powder shows a lognormal distribution with a D0.5 at 37.4 μm and a span of 0.622.

The morphological analysis of the Mar-M-247 and the CM 247 LC powder materials promises a satisfying

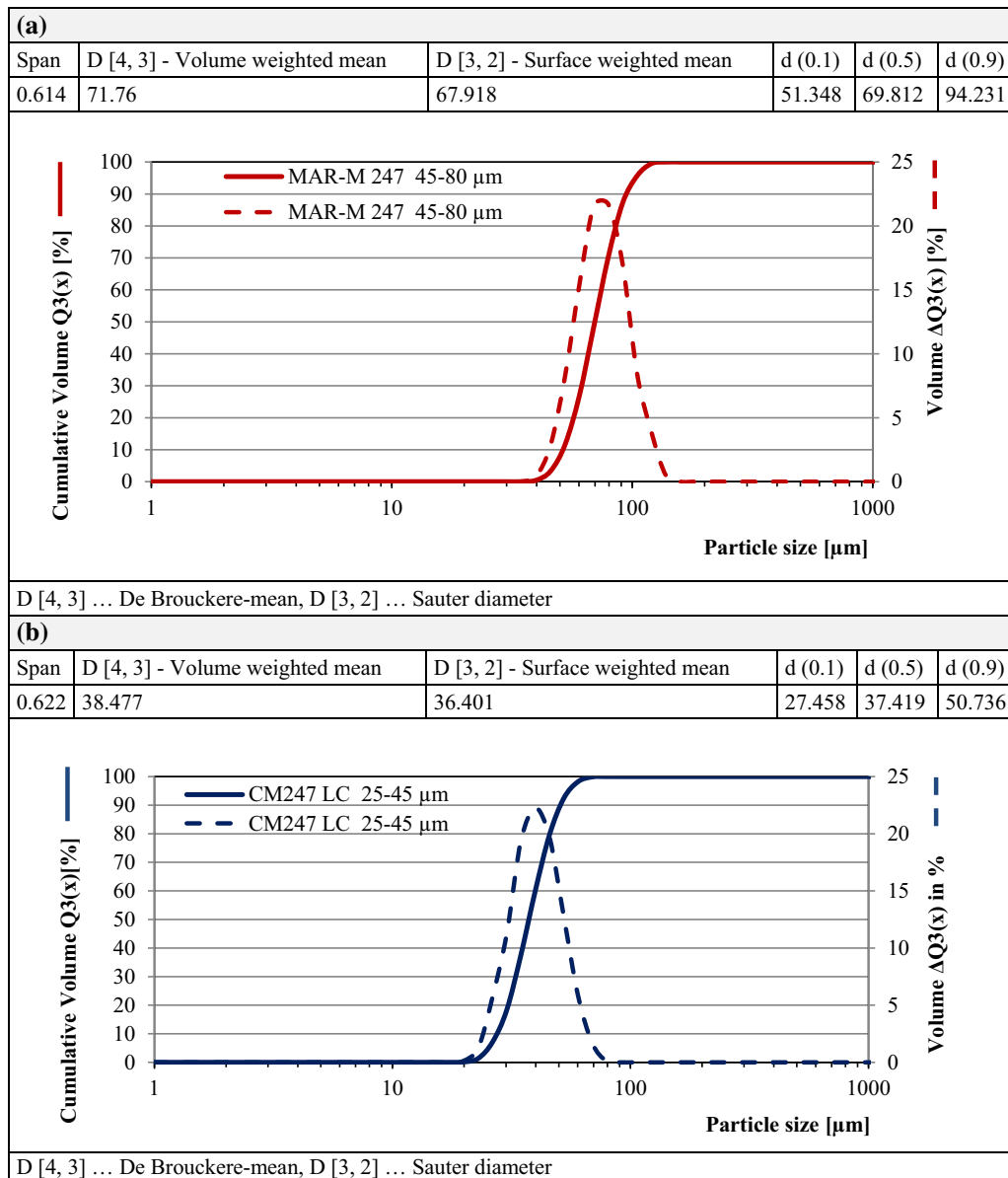


Fig. 9—Results from the particle size distribution measurements with laser diffraction for (a) Mar-M-247 powder with nominal size range of 45 to 80 μm . (b) CM 247 LC powder with nominal size range of 25 to 45 μm .

processability with LMD. The spherical particles with rather limited fine satellites and the narrow uniform particle size distribution of the powders typically result in good processability in terms of flow ability. Furthermore, both powder materials show a low porosity leading to a low porosity of the volumes after processing. Because of the existing particle size distributions, different flowing parameters can be expected. In either way, the powders comply with the requirements.

1. Chemical composition

The chemical composition of the alloying elements was measured *via* inductively coupled plasma optical emission spectrometry (ICP-OES), inductively coupled plasma atomic emission spectroscopy (ICP-AES), and pyrolysis infrared spectroscopy (Py-IR). The latter was

used as supporting techniques to determine the carbon content (see Table II).

Looking at the results of Mar-M-247, it can be seen that the mass fractions of the majority of the alloying elements correspond with the nominal compositions. Larger deviations occurred only at the boron content. However, in the literature, the weldability is often linked to the content of the strengthening elements Al and Ti.^[43–46] Hence, the increased mass percentages of these elements are assumed to further reduce the weldability.

On the other hand, CM 247 LC shows larger deviations especially at the Al- and Ti-contents. Furthermore, the reduced mass percentages of the latter elements seem likely to work in favor for the weldability. Nevertheless, the measured proportion is still above what is considered as weldable.^[43–46]

Table II. Result from ICP-OES/ICP-AES and Pyrolyse-IR Measurements at Mar-M-247 and CM 247 LC Powder Particles in Weight Percent

	Ni	Co	W	Cr	Al	Ta	Hf	Ti	Mo	C	Zr	B
Mar-M-247*	59.59	9.86	10.20	8.10	5.69	3.00	1.57	1.03	0.69	0.06	0.03	0.18
Δ Wi**	—	- 0.14	+ 0.20	- 0.15	+ 0.19	+ 0.00	+ 0.07	+ 0.03	- 0.01	- 0.09	- 0.02	+ 0.17
CM 247 LC*	62.41	8.97	10.57	7.88	4.20	3.08	1.62	0.68	0.46	0.01	0.03	0.08
Δ Wi**	—	- 0.23	+ 1.07	- 0.22	- 1.40	- 0.12	+ 0.22	- 0.02	- 0.04	- 0.06	+ 0.01	+ 0.07

*Ni, Co, W, Cr, Al, Ta, Hf, Ti, Mo, Zr, B measured *via* ICP-OES/ICP-AES; C measured *via* Py-IR.

**Delta of measured value of the mass fraction and the nominal mass fraction.

Table III. Process Parameters for the Hybrid LMD of Mar-M-247 and CM 247 LC

	Substrate Surface Temperature (°C)	Laser Power (W)	Powder Mass Flow (g/min)	Carrier Gas Volume Flow (L/min)	Shielding Gas Volume Flow (L/min)	Feed Rate (mm/min)
Mar-M-247	900	400	2	6	10	500
CM 247 LC	900	550	1.7	6	10	500

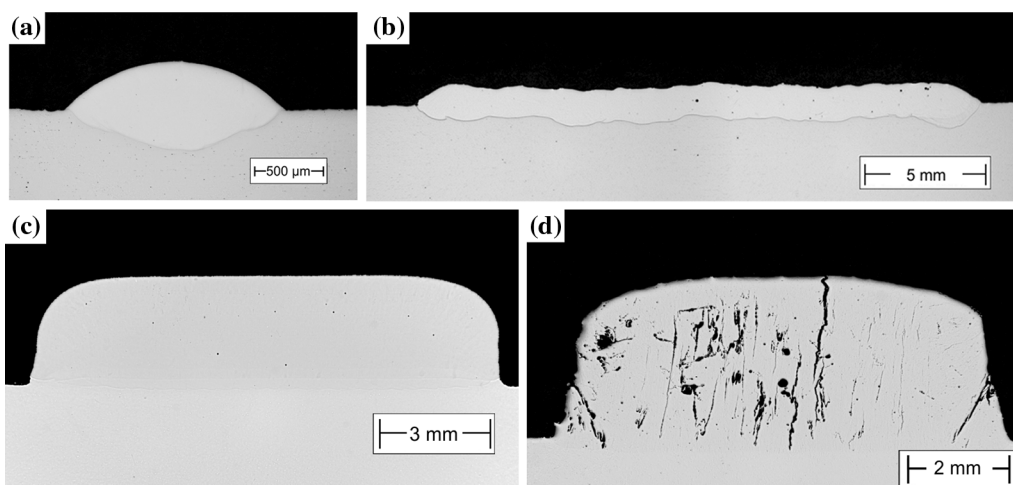


Fig. 10—Metallographic cross sections of Mar-M-247 manufactured on the same type substrate with appropriate thermal tailoring shown in the as-built condition (without heat treatment or hot isostatic pressing) presenting a single weld bead (a), a single layer (b), and a multilayer volume (c). (d) Comparative sample manufactured without thermal tailoring.

B. Process Development

The powdery filler metal is delivered into the process zone by means of an inert carrier gas (argon) as indicated in Figure 5. Along this path, it is preheated in the laser beam and finally reabsorbed into the laser-induced melt pool on the preheated substrate material (surface temperature at approximately 900 °C). The used laser sources were a 1000 W solid-state laser with 1030 nm wavelength (Trumpf Trudisk 1000) and a wavelength-coupled diode laser with maximum 4000 W and an wavelength between 900 and 1070 nm (Laserline LDF 4000-30). The initial laser power can be seen in Table III in which the power was regulated using the »E-MAqS« system in order to prevent heat accumulation (see Figure 6).

Analogous to this, the heat input in the substrate material was regulated as described above. The process parameter sets were subjected to comprehensive analysis addressing the investigation of the absence of cracks, the

grain size, and the grain size distribution *via* metallographic examination. Figure 10 indicates the process development showing a single weld bead, a single layer, and a multilayer volume. The results of this study are shown in the as-built condition (no HT or HIP), and it is apparent that the representative samples in Figures 12(a) through (c) show small porosity, but the absence of cracks. In contrast to this, the sample shown in Figure 10(d), which was manufactured without thermal tailoring for comparison, shows comprehensive solidification cracking.

Based on this, suitable process parameters were derived for the hybrid manufacturing of volume elements (Table III).

The LMD processing heads, developed at Fraunhofer IWS, are integrated in modern 5-axis machining centers of the type Hermle C 800 and DMG Mori LASERTEC 65 3D hybrid.

C. Additively Manufactured Parts, Thermal Treatments, and Materials Samples

Solid volume samples were manufactured layerwise (Figure 11(a)). These samples have a height of approximately 53 mm and a diameter of approximately 13 mm and were achieved by the deposition of 104 layers each with a respective thickness of approximately 500 μm . Each layer consists of a contour weld and bidirectional filler weld beads. The orientation of consecutive layers was continuously rotated by 45 deg during the whole material build-up (cf. Figures 23(c) and (d)). After the hybrid manufacturing hot isostatic pressing (HIP) was carried out as the first step of thermal treatment. This was performed in order to enable a better comparability with the literature data. However, it was a one-step procedure at 200 bars with a dwell time of 4 hours at 1200 $^{\circ}\text{C}$ (see Figure 11(b)).

After HIP the samples were solution annealed and aged in a high vacuum furnace according to Hsu *et al.*^[33] The solution heat treatment (1232 $^{\circ}\text{C} \pm 10^{\circ}\text{C}$ for 2 hours) was followed by a first aging step

(1080 $^{\circ}\text{C} \pm 10^{\circ}\text{C}$ for 2 hours) and a second aging step (870 $^{\circ}\text{C} \pm 10^{\circ}\text{C}$ for 20 hours). During the entire heat treatment procedure, the sample temperature did not fall below 540 $^{\circ}\text{C}$ (see Figure 12).

Tensile test specimens were prepared from hybrid manufactured samples as well as from an ingot. All samples were treated with HIP (according to Figure 11(b)), solution annealed and aged (according to Figure 12), and prepared by wire-cut electrical discharge machining. The tensile tests were performed in the as-cut surface condition in order to avoid mechanical exposure before testing. The design of the tensile samples was followed conforming to DIN 50125-B standards.

D. Hot Tensile Testing, Fracture Surfaces, and Computer Tomography

Tensile testing was performed according to Reference 34 at a temperature of 760 $^{\circ}\text{C}$ with a preload of 10 N and a test speed of 0.4 mm/min. The temperature was

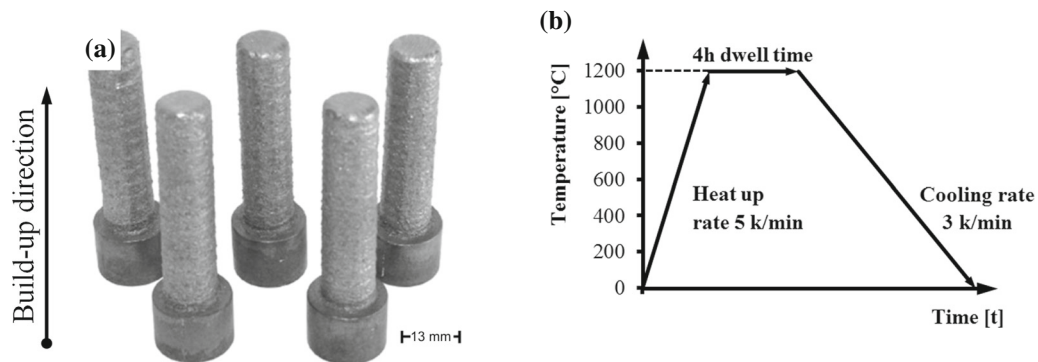


Fig. 11—(a) Samples of hybrid LMD manufactured parts of Mar-M-247 on a Mar-M-247 ingot substrate. (b) Presentation of the thermal cycle of the hot isostatic pressing (HIP) which was carried out at a pressure of 200 bar.

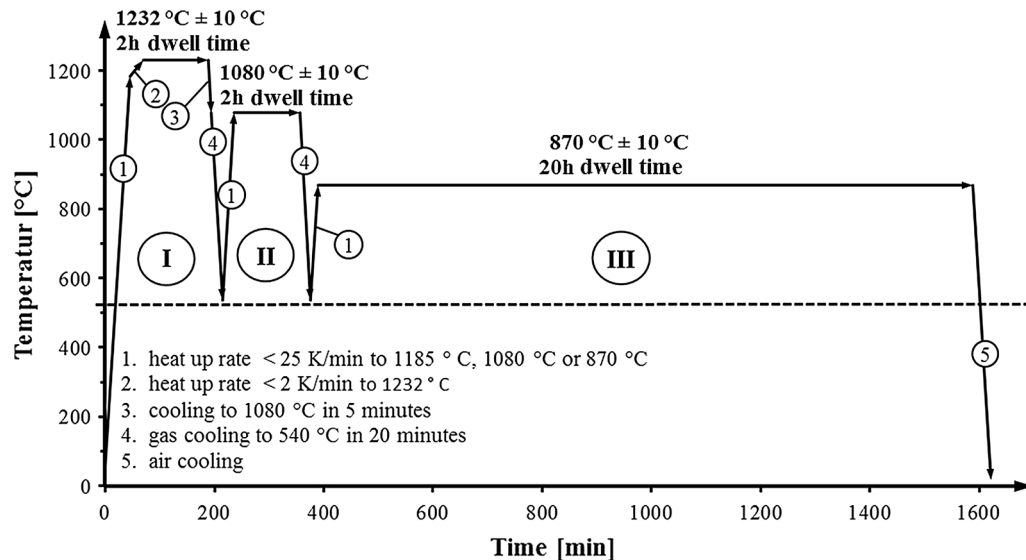


Fig. 12—Heat-treatment procedure for Mar-M-247 and CM 247 LC according to Hsu *et al.*^[33]

chosen in accordance with References 35 and 36. The test campaign comprised the testing of eight tensile specimens of which four came from the Mar-M-247 ingot and four were manufactured additively. The resulting stress–strain curves, obtained at elevated temperature, are summarized in Figures 13(a) and (b). The tests were performed using a universal testing machine, Zwick 1476, in a laboratory atmosphere.

Detailed results of the other samples are shown in Table IV.

The hybrid AM specimens showed a superior Rp0.2 yield strength, ultimate tensile strength, and elongation at fracture (see Table IV). These specimens reached an average elastic modulus of 161 GPa, an average ultimate tensile strength of ~ 980 MPa, and an average elongation at fracture of ~ 5 pct. These values are comparable to the values given in the pertinent literature.^[3,37] Nevertheless,

the absolute values of the elongation vary from sample to sample from 3 to 7 pct (see Table IV). The ingot material exhibits a lower average elastic modulus of ~ 108 GPa, a tensile strength of just 918 MPa, and an elongation at fracture of 3.3 pct. These values are in principle worse than the results of the hybrid AM specimens but also worse than comparative figures in the literature.^[40–42] The latter provides for MAR-M247 ingot material with HIP an elastic modulus of ~ 187 GPa, a Rp0.2 yield strength of 782 MPa, a tensile strength of 1027.87 MPa, with an elongation at fracture of 5.061 pct for a testing temperature of 750 °C. In either way, ingot and hybrid materials reveal a big scatter of the yield strength at extensometer elongation of 0.2 pct and elongation at fracture.

This hypothesis, however, needs to be statistically verified by a higher number of specimens. For this purpose, the absolute values shall be examined in detail.

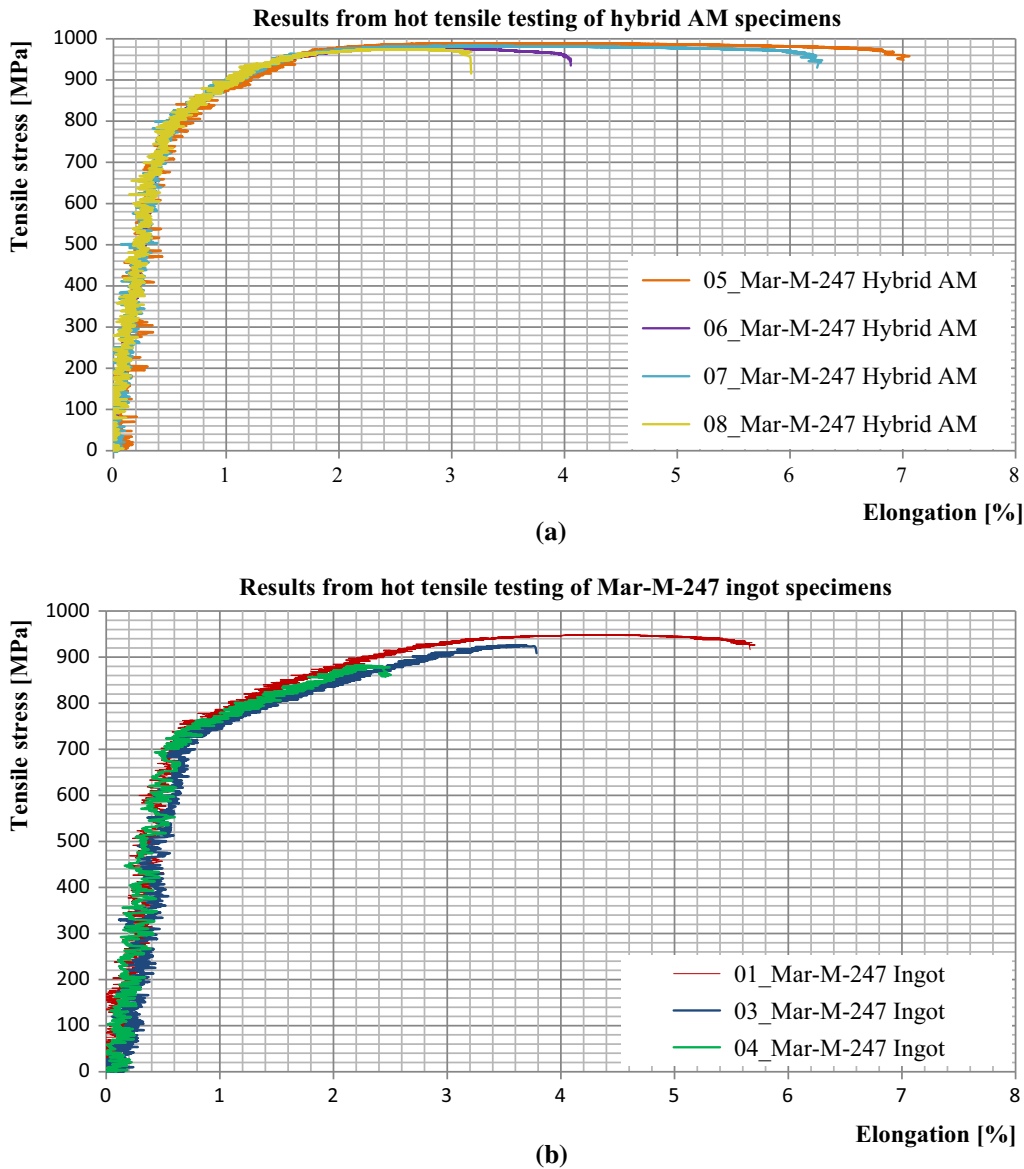









Fig. 13—(a) Stress–strain curves of the hybrid AM Mar-M-247 specimens, HIP treated (according to Fig. 11) and heat treated (according to Fig. 12), obtained at a test temperature of 760 °C ± 5 °C. (b) Stress–strain curves for Mar-M-247 ingot specimens, HIP treated (according to Fig. 11) and heat treated (according to Fig. 12), obtained at a test temperature of 760 °C ± 5 °C (Color figure online).

Table IV. Results from the Tensile Testing of the Mar-M-247 Test Specimens at a Temperature of 760 °C (Color table online)

Legend	Label	S_0 (mm ²)	mE (GPa)	Rp0.2 (MPa)	Fm (kN)	Rm (MPa)	Ag (Pct)	A (Pct)
	01_Mar-M-247 Ingot	12.60	106	114	11.94	948	3.65	5.1
	03_Mar-M-247 Ingot	12.61	106	742	11.66	925	2.75	2.9
	04_Mar-M-247 Ingot	12.70	114	70	11.21	882	1.48	1.8
	05_Mar-M-247 HybridAM	12.20	179	775	12.07	989	3.13	7.0
	06_Mar-M-247 HybridAM	12.60	165	824	12.30	977	2.30	3.8
	07_Mar-M-247 HybridAM	12.60	153	827	12.38	983	2.63	6.4
	08_Mar-M-247 HybridAM	12.57	147	815	12.24	974	1.90	2.8

Testing of sample 02_Mar-M-247 Ingot was invalid.

S_0 : initial cross section, mE: slope of HOOKE lines (DIN EN ISO 6892-1, Rp0.2: yield strength (yield strength at extensometer elongation of 0.2 pct), Rm: tensile strength, Ag: uniform elongation, A: elongation at fracture, Fm: maximum load.

With the current data, it seems likely that the worse results obtained from the comparative ingot material can be attributed to the considerably more inhomogeneous microstructure. After all, the hybrid AM specimens showed promising mechanical properties even when compared with the literature data.

Fracture surfaces were investigated by scanning electron microscopy (see Figure 14). Higher magnifications identified large differences of the microstructures between the cast ingot and the specimens manufactured *via* hybrid LMD.

As expected, the ingot shows rather large metal carbides and inhomogeneous γ' precipitates in terms of shape, size, and distribution. These carbides and precipitates can be recognized by their splintered appearance indicating that they exhibit a brittle fracture behavior. The surrounding matrix apparently shows a mainly ductile, transgranular fracture, as can be verified from the presence of numerous pits and dimples with a honeycomb-like structure on the fractured surfaces of both, the ingot and the additively manufactured specimens. However, the pits in the additively manufactured samples are much smaller and more homogeneously distributed than those in the cast material. It is conspicuous that the carbides can always be found in the center of those dimples, which are especially noticeable in Figures 14(c) and (b). This provides evidence that the precipitates act as internal notches promoting crack initiation. The crack is then formed by the coalescence of those microvoids. At lower magnifications, a meandering crack is visible in the ingot material (Figure 14(a)). It seems plausible that this crack runs along the brittle interdendritic areas (see Figures 4 and 7). Nevertheless, similar cracks can be found in the additively manufactured specimens (Figure 14(b)) but with a shorter length. Furthermore, the fractured surfaces appear more uniform compared with the ingot samples, presumably due to the finer carbides and γ' precipitates, which are also likely to be the cause for the observed overall higher elongation at fracture during tensile testing (Table IV).^[38] However, this microstructure may change during service.^[39] The density of the samples was investigated *via* X-ray computer

tomography. The minimum detection limit of the applied method is 10 μm . The analysis was made through X-ray computer tomography equipment YXLON FF35 CT, equipped with the reconstruction software YXLON ReconsPOOLer version 1.2.1.0 and the software VGStudio MAX 3.0 for the nominal/actual comparison and porosity analysis. As expected, the ingot shows no macrospores and minor micropores (see Figure 15), which can be explained by the manufacturing performed under vacuum and the HIP treatment of the samples (see Figure 11). In contrast, the hybrid AM samples showed more microporosity (Figure 15). The presence of microporosity can be explained through the application of carrier and shielding gas (see Figure 5), which leads to gas encapsulations which cannot be closed during the HIP treatment.

These findings were confirmed by several measurements. The results for the specimen 04 Mar-M-247 (ingot) show a total defect volume of approximately 0.1 mm³ for a material volume of 406.46 mm³. On the other hand, there is the hybrid AM sample 07 Mar-M-247 which shows a total defect volume of approximately 0.108 mm³ for a material volume of 177.79 mm³. Considering that the size of hybrid sample volume is only 43.7 pct of the size of the ingot volume, the higher porosity becomes obvious as well. Nevertheless, all the samples showed a very low total porosity independent of the fabrication method.

E. Electron Backscattered Diffraction, Scanning Electron Microscopy, and Metallographic Examination

For a detailed analysis of the microstructure and its crystallographic orientation, electron backscattered diffraction (EBSD) measurements were performed at longitudinal sections after tensile tests. Samples were embedded, ground, diamond polished, and finally polished with OP-S (Struers). Measurements were done on a FEG-SEM ULTRA 55 Plus (Zeiss) machine attached with an EBSD system Channel5 with detector Nordlys F (Oxford Instruments). SEM conditions were 20 kV, beam current of about 7 nA, sample tilted to 70 deg with distance 15 mm, and pattern recorded with 20 to

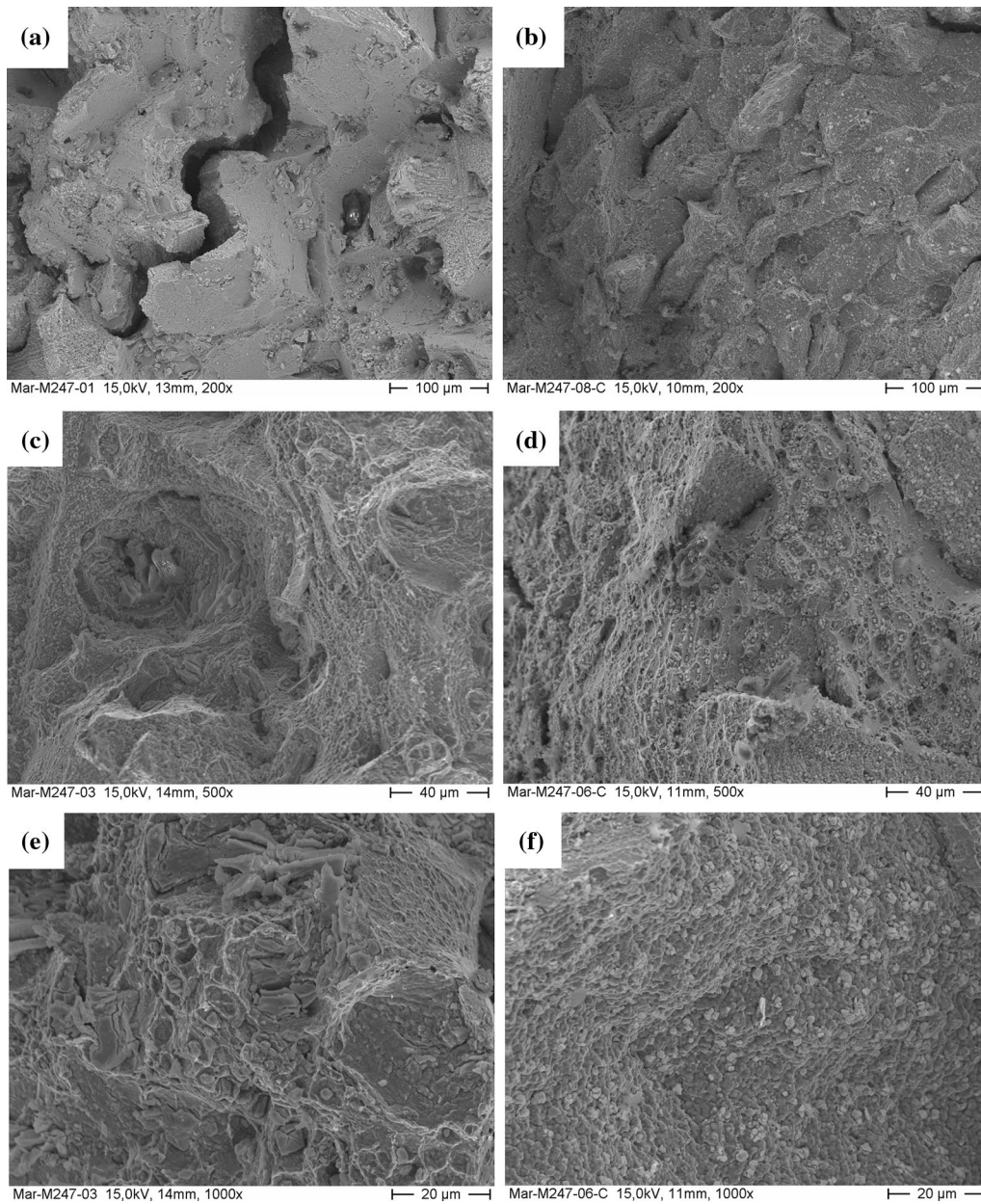


Fig. 14—SEM images of the Mar-M-247 ingot tensile test specimens and the hybrid AM tensile test specimens all HIP treated (according to Fig. 11) and heat treated (according to Fig. 12) obtained from testing at a test temperature of $760 \text{ }^\circ\text{C} \pm 5 \text{ }^\circ\text{C}$ for showing (a) fracture surface of ingot tensile test specimen 01_Mar-M-247, (b) fracture surface of hybrid AM tensile specimen 08_Mar-M-247, (c) fracture surface of ingot tensile test specimen 03_Mar-M-247, (d) fracture surface of hybrid AM tensile specimen 06_Mar-M-247, (e) fracture surface of ingot tensile test specimen 03_Mar-M-247, and (f) fracture surface of hybrid AM tensile specimen 06_Mar-M-247.

40 ms. Samples were treated as single-phased fcc Ni with Ni fcc lattice (m-3m, SG 225, $a = 352 \text{ } \mu\text{m}$) because the Ni₃Al- phase with $a = 357 \text{ } \mu\text{m}$ is too similar to be distinguished by EBSD patterns. For each sample, three orientation maps were recorded with a point distance of $3 \text{ } \mu\text{m}$ and a grid size of $1.8 \times 1.2 \text{ mm}$. In Figure 16, examples of EBSD orientation maps are illustrated showing the crystal directions in building direction using inverse pole figure coloring (all HybridAM images perpendicular to the build-up direction).

It is evident that the microstructure of cast ingot is very coarse-grained, and the grain sizes are in the range of 500 to $> 1000 \text{ } \mu\text{m}$. In contrast, the samples produced

by LMD reveal a complex and heterogenous grain structure with bundles of strongly elongated grains (100 to $600 \text{ } \mu\text{m}$ long, 30 to $100 \text{ } \mu\text{m}$ wide), numerous smaller, equiaxed grains beyond $50 \text{ } \mu\text{m}$, and added by some big grains larger than $200 \text{ } \mu\text{m}$, with lower elongation. The analyzed areas (3 maps of 2.5 mm^2 each) show no distinctive texture. The peaks in the inverse pole figures of all the samples did not exceed values of 4 m.u.d. and were mostly induced by the biggest grain.

Comprehensive metallographic examination was carried out. Figure 17 shows representative scanning electron microscope images taken from samples with the surface preparation for the EBSD investigations. In

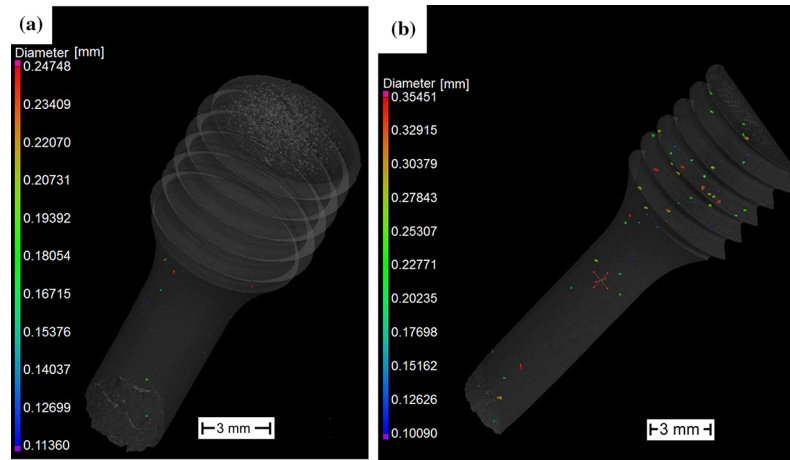


Fig. 15—(a) X-ray CT measurement of the Mar-M-247 ingot tensile test specimen 04_Mar-M-247 and (b) X-ray CT measurement of the Mar-M-247 HybridAM tensile test specimen 07_Mar-M-247 all HIP treated (according to Fig. 11) and heat treated (according to Fig. 12) (Color figure online).

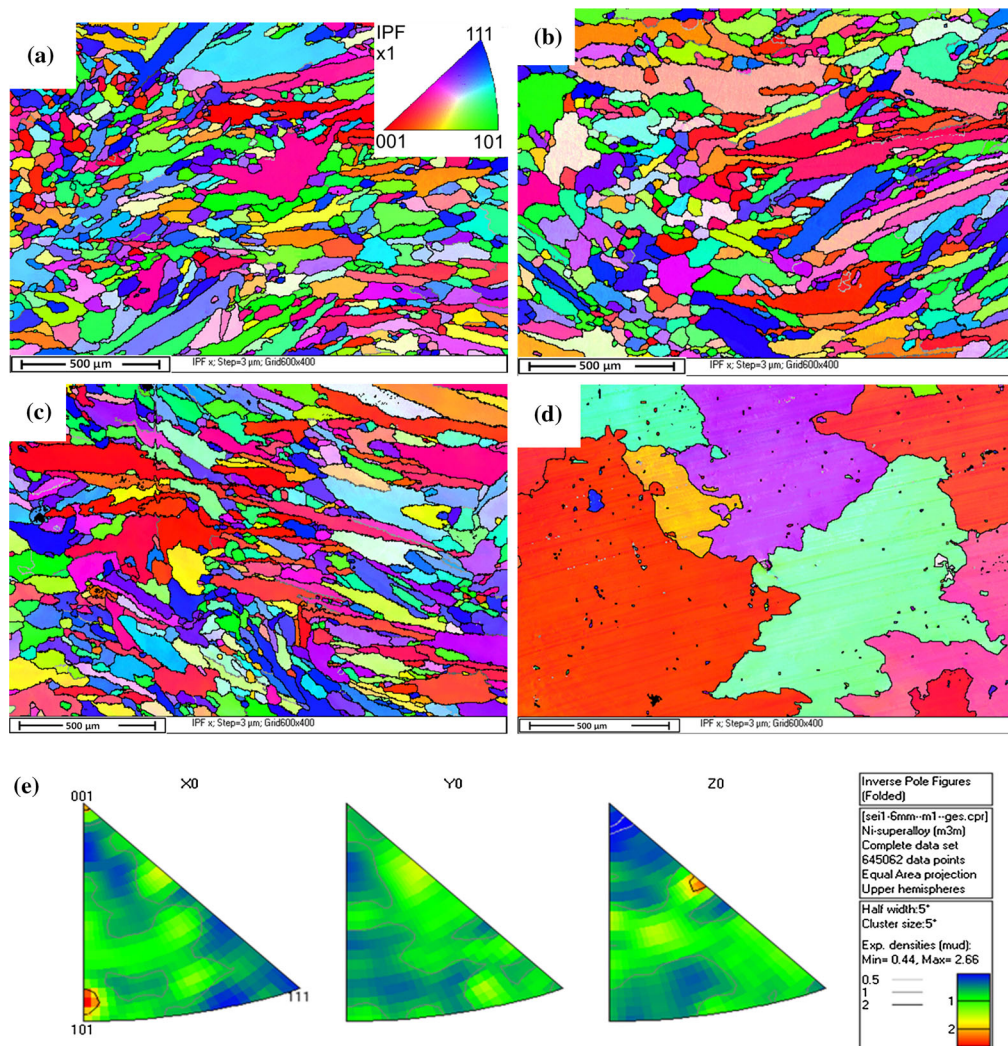


Fig. 16—EBSD maps of Mar-M247 samples displaying the orientational component in building direction, IPF coloring of hybrid AM Samples 03_Mar-M-247, 05_Mar-M-247, and 08_Mar-M-247 (a through c), and the ingot sample 03_Mar-M-247 Ingot (d), statistically evaluated inverse pole figures from all maps of sample 05_Mar-M-247 HybridAM [IFW-P2], and (e) Contourized inverse pole figure sample 05_Mar-M-247 HybridAM [IFW-P2] (Color figure online).

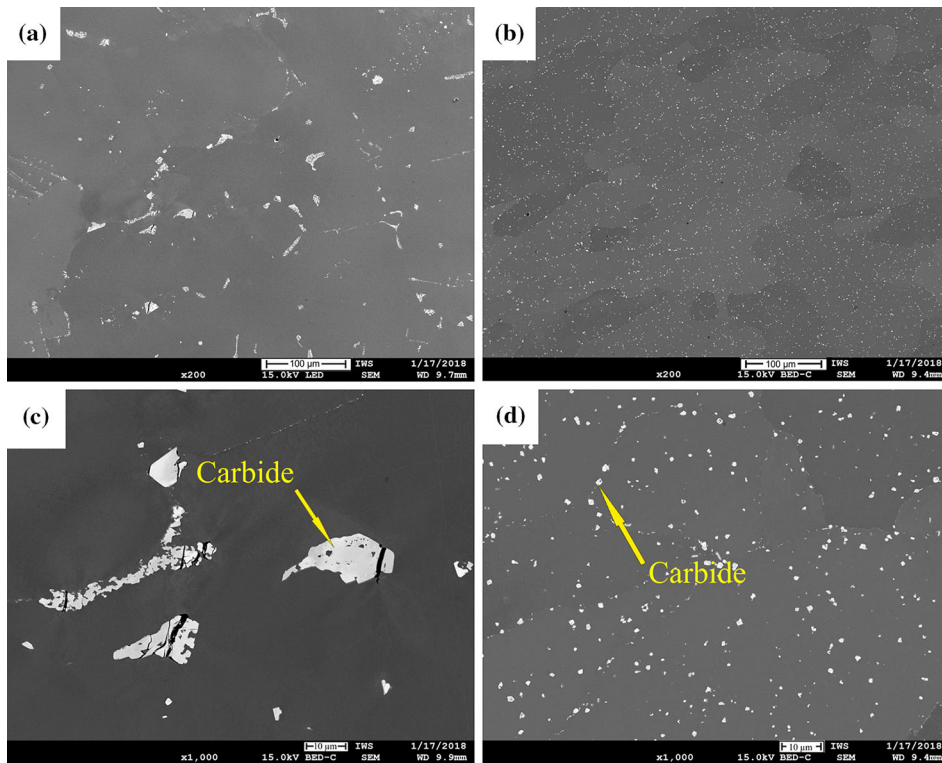


Fig. 17—SEM images of metallographic sections (a and c) Mar-M-247 ingot tensile test specimen 03_Mar-M-247. (b and d) Mar-M-247 HybridAM tensile test specimen 08_Mar-M-247.

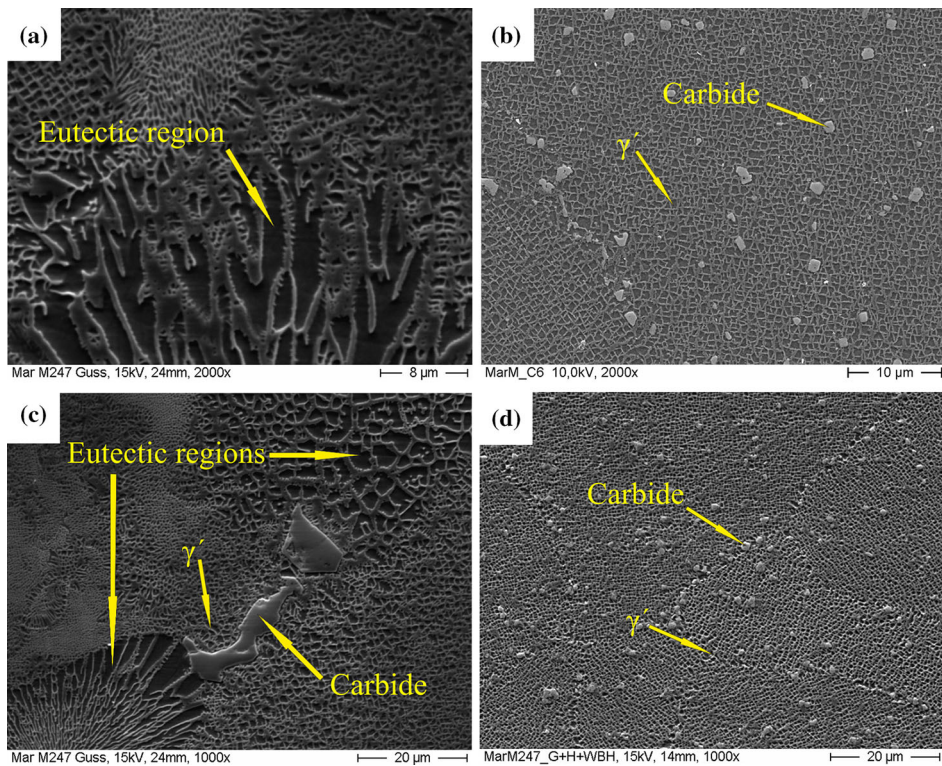


Fig. 18—(a, c) SEM images of the Mar-M-247 ingot material showing the inhomogeneous multiphase microstructure with the γ' precipitates of Ni_3 (Al,Ti,Ta) (dark) in the γ -matrix (gray) and strip-type carbides (light-gray); (b, d) Mar-M-247 HybridAM tensile test specimen 06_Mar-M-247 and 08_Mar-M-247 with γ' precipitates of Ni_3 (Al,Ti,Ta) (dark) in the γ -matrix (gray) and cuboidal carbides (light-gray).

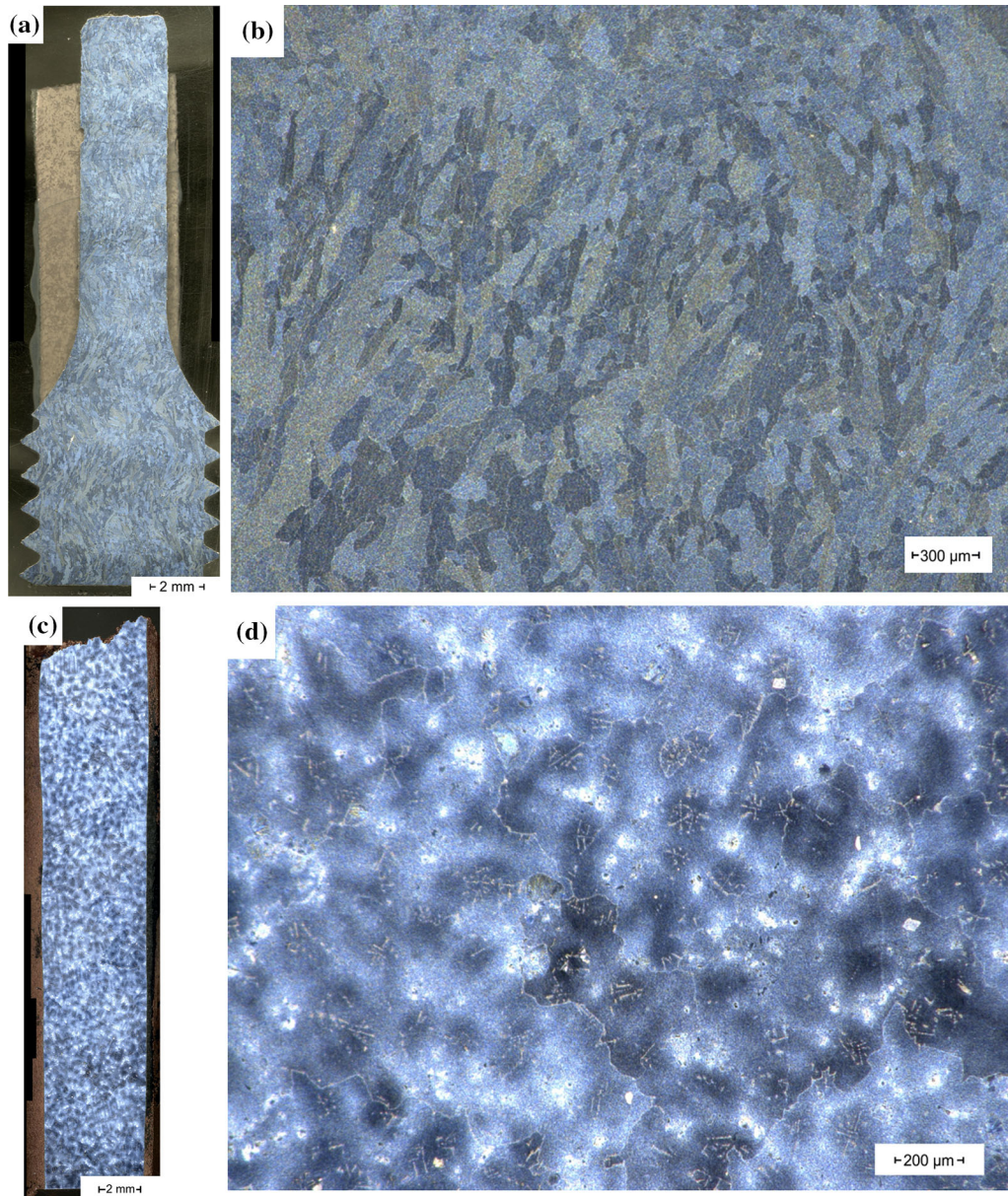


Fig. 19—(a) Cross section (perpendicular to build-up direction) for the light optical microscope evaluation of the hybrid LMD tensile sample 08_Mar-M-247 with 50 x magnification. (b) Detail with $\times 200$ magnification. (c) Cross section for the light optical microscope evaluation of the Mar-M-247 ingot material tensile sample 03_Mar-M-247 with $\times 50$ magnification. (d) Detail with $\times 200$ magnification (right). All pictures were taken using a digital microscope Keyence VHX (Color figure online).

accordance with the observations of the fractured surfaces (see Figure 14), it can be confirmed that the metal carbides of the ingot are larger and noticeably more inhomogeneous in terms of shape, size, and distribution when comparing the samples manufactured *via* hybrid AM. Obviously, the carbide precipitates are considerably smaller and more uniform in the hybrid samples than in ingot specimens. All HybridAM images are shown perpendicular to the build-up direction.

Further investigations confirmed large differences of the microstructure between the cast ingot and the specimens manufactured *via* hybrid LMD with powder (see Figure 18). It can be seen that the ingot consists of rather inhomogeneous cellular structured areas with

$\gamma - \gamma'$ eutectics. Furthermore, the size and morphology of the γ' precipitates show considerably greater range, and elongated carbides are present. In contrast, the hybrid AM specimens show no distinct $\gamma - \gamma'$ eutectics and the γ' precipitates, as well as that the cuboidal carbides are uniform in terms of size and shape.

Figure 19 shows a cross section of a hybrid AM tensile sample of Mar-M-247 after the testing at elevated temperatures. The right side of the figure shows a magnification of the microstructure of the hybrid AM sample 08_Mar-M-247, which corresponds to the findings from electron backscattered diffraction (see Figure 16). In comparison, the results for the ingot sample 03_Mar-M-247 can be seen in Figure 19 too. It is

clearly visible that the grains of the sample produced from the ingot are larger than the grains of the samples manufactured *via* hybrid AM. Furthermore, there are large numbers of areas with $\gamma - \gamma'$ eutectics with very bright appearance (Figures 19(c) and (d)).

III. HYBRID PROCESSING OF CM 247 LC

A. Process Development

Analogous to the process development with Mar-M-247, the processing of CM 247 LC has been subjected to comprehensive analysis addressing the investigation of the absence of cracks. The characteristics of the powdery filler material were described earlier. The developed process parameters are shown in Table III. The process development included the manufacturing of weld beads and single layers and multilayer volumes. The dense cubes shown there were treated with HIP (according to Figure 11) and heat treated (according to Figure 12), and it is apparent that the representative samples show small porosity but the absence of cracks (Figure 20). However, the absence of cracks is also shown in the as-build condition without HT or HIP (see Figure 24).

The density of the samples was investigated *via* X-ray computer tomography. The samples did not show any macropores and minor micropores within the hybrid-manufactured volumes (see Figure 21). This is in line with the results from the metallographic investigations (see Figure 21). Nevertheless,

the CT results need to be critically evaluated because of the comparatively large volume in combination with the high density of the material. On the other

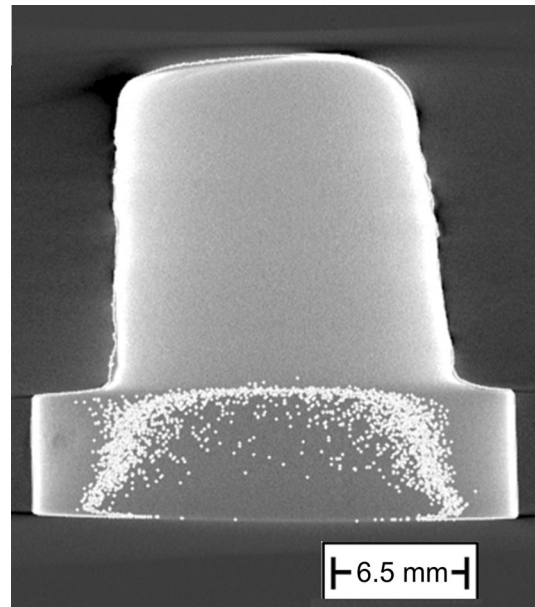


Fig. 21—X-ray CT measurement of the CM 247 LC multilayer volume density cube in the as-build condition (without heat treatment or hot isostatic pressing) showing no macropores and minor micropores within the hybrid-manufactured volume but several micropores within the Mar-M-247 substrate material (ingot).

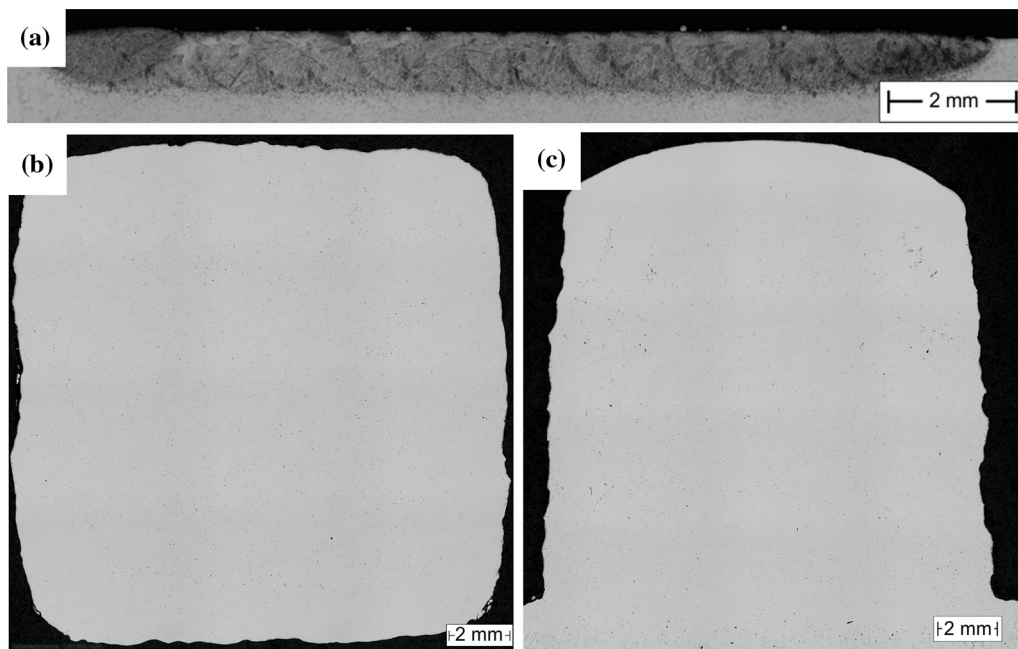


Fig. 20—Investigation of the absence of cracks at metallographic cross sections of CM 247 LC manufactured with appropriate thermal tailoring on a Mar-M-247 ingot substrate presenting. (a) A single weld bead in the as-build condition (without heat treatment or hot isostatic pressing). (b) A multilayer volume cut parallel to the build-up direction. (c) A multilayer volume treated with HIP (according to Fig. 11) and heat treated (according to Fig. 12) cut perpendicular to the build-up direction.

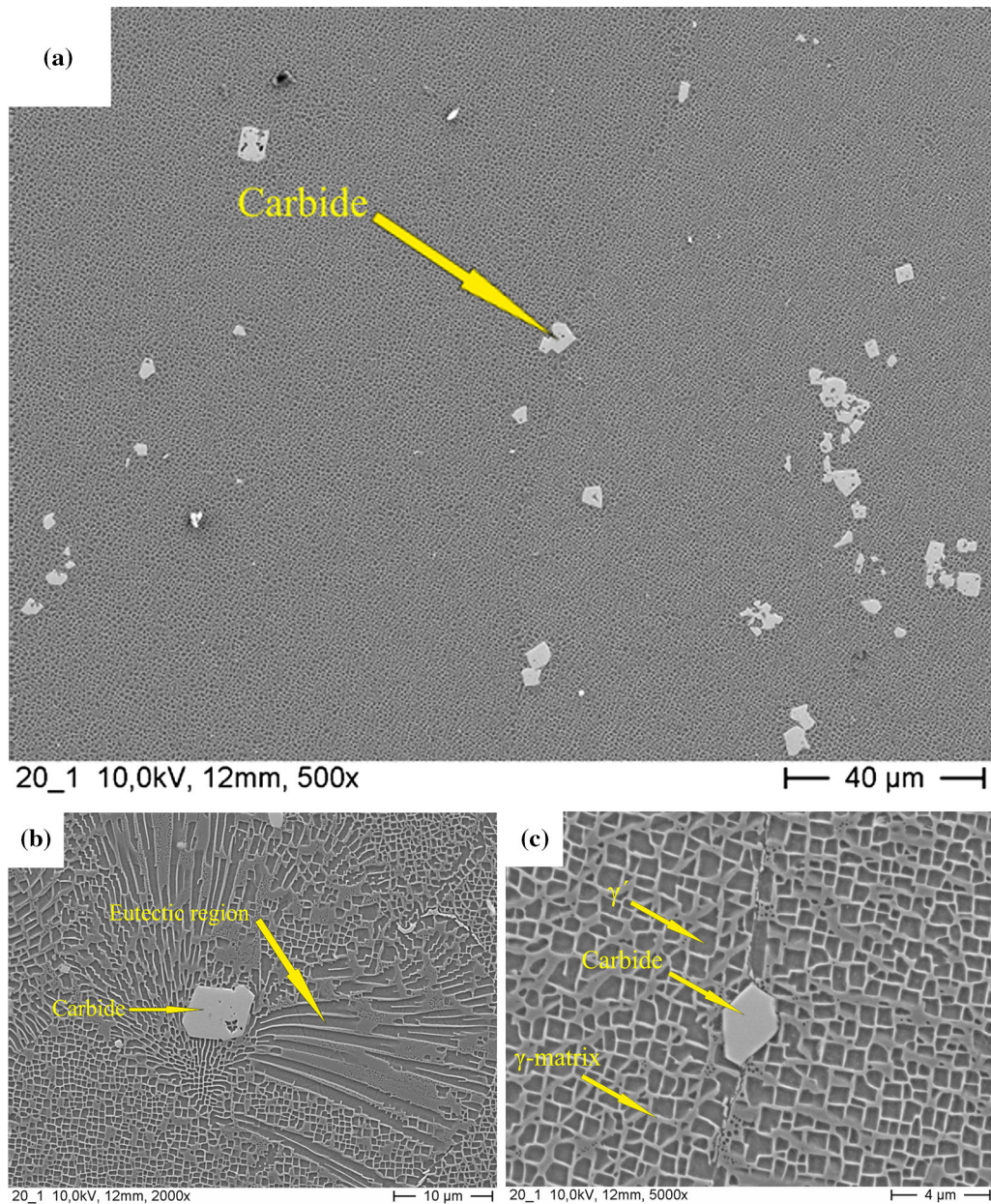


Fig. 22—SEM images of micrographs of hybrid manufactured CM 247 LC material treated with HIP (according to Fig. 11) and heat treated (according to Fig. 12) showing (a) the homogeneous multiphase microstructure with the γ' precipitates of $\text{Ni}_3(\text{Al,Ti,Ta})$ (dark) in the γ -matrix (gray) and block-type carbides (light-gray). (b) A eutectic region with the γ' precipitates of $\text{Ni}_3(\text{Al,Ti,Ta})$ (dark) in the γ -matrix (gray) and block-type carbides (light-gray). (c) Corresponding detail with 5000 x magnification.

hand, micropores were observed in the substrate material.

Further investigations showed a rather homogeneous size and morphology of the γ' precipitates and small regions with $\gamma - \gamma'$ eutectics (see Figure 22).

B. Demonstrator Parts

Based on the previous results, the manufacturing of more complex demonstrator parts was addressed. With regard to typical applications, a twisted turbine blade

was chosen as reference geometry. Analogous to the basic experiments, the surface temperature was held at approximately 900 °C (see Table III). In order to compensate the temperature drop at the leading edge and the trailing edge (Figure 23(b)), the preheating temperature was increased to 1100 °C. Following this, CM 247 LC volumes were manufactured with the parameters shown in Table III. Each layer consists of a contour weld and bidirectional filler weld beads (Figure 23(c)). According to the previous investigations, the orientation of consecutive layers was conducted

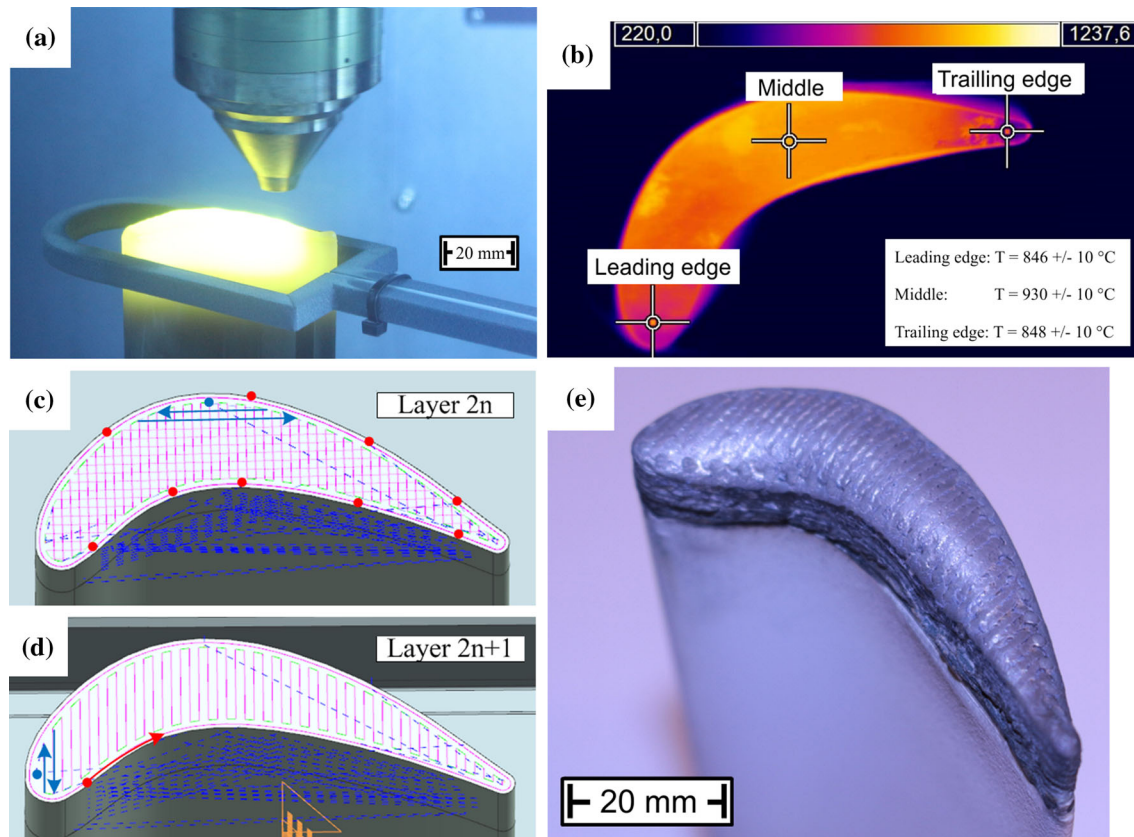


Fig. 23—(a) Presentation of the inductive heating of the twisted turbine blade substrate. (b) Corresponding qualitative temperature distribution with measuring points at the leading edge, in the middle, and the trailing edge showing the temperature data measured using a pyrometer. (c) Illustration of the welding strategy with a surrounding contour weld (red arrow) and bidirectional filler weld beads (blue arrow) (d) Rotation of consecutive layers from layer $2n$ to layer $2n + 1$ by 90 deg. (e) Result after the hybrid material build-up (Color figure online).

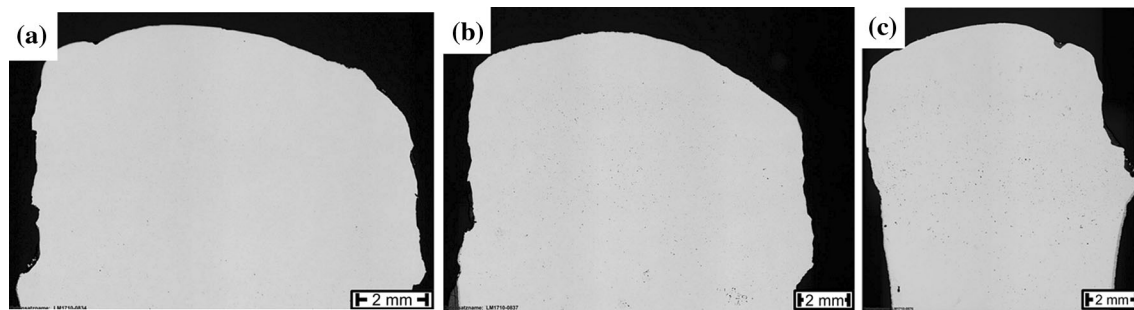


Fig. 24—Metallographic investigation of the absence of cracks of a hybrid-manufactured, twisted CM 247 LC turbine blade shown in the as-build condition (without heat treatment or hot isostatic pressing) with cross sections from (a) the leading edge, (b) the middle part, (c) the trailing edge.

under continuous rotation (Figure 23(d)). The rotation was done by 90 deg during the whole material build-up. The experiments were performed using a DMG-Mori LASERTEC 65 3D. The latter 5-axis machining center uses a coaxial nozzle (Figure 23(a)) developed by Fraunhofer IWS. Furthermore, Eldec MICO L mid-frequency energy source with a maximum power level of 80 kW was used for the coupling of energy sources.

During this stage of the investigation, the »E-MAqS« sensor system was not used in order to maintain the thermal balance of the process. This was done in order

to evaluate the geometrically induced accumulation of heat toward the influence on the contour accuracy. However, no cracks could be seen at the representative metallographic sections (see Figure 24).

The results of the test agree with the findings from the process development, where these results were achieved during the manufacturing of dense cubes (see Figure 20), as well as with the results from Mar-M-247 (see Figure 10). In either way, the contour accuracy can be significantly improved *via* targeted control of the total energy input (see Figure 6). The potential of an

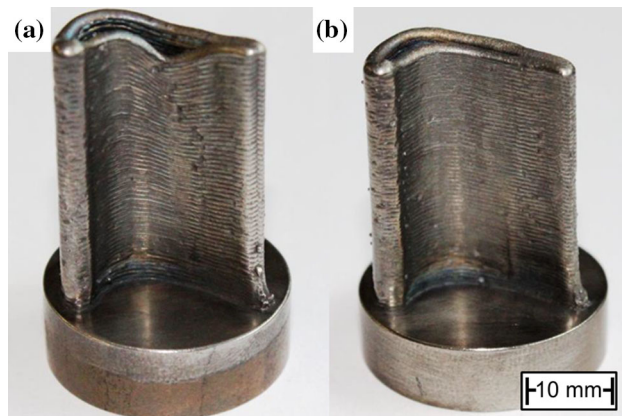


Fig. 25—Miniaturized demonstrator of a turbine blade with low wall thickness and limited lateral extent manufactured: (a) Without temperature control and (b) with temperature control.

intelligent heat control can be illustrated with the miniaturized demonstrator of a turbine blade as shown in Figure 25. The demonstrator was manufactured *via* hybrid LMD from the Mar-M-247 powder material. The dimensions were chosen as a worst-case scenario in terms of the accumulation of heat or geometrical precision, respectively. However, it can clearly be seen that the geometric fidelity was drastically improved *via* the application of appropriate temperature control. Currently, these results are transferred to complex three-dimensional (3D) structures with representative dimensions.

IV. SUMMARY

The present paper addresses the investigation of hot cracking of Ni-based superalloys within the perspective of hybrid LMD. Starting with dimensional factors and different approaches toward the avoidance of hot crack formation, the laser-induced melt pool is examined in terms of its specific characteristics. The solidification process was analyzed with particular consideration of the microstructure and the chemical composition. The development and application of tailored temperature cycles in synergistic interaction with the appropriate system technology (process tailoring) leads to a better control of shrinkage stresses.

The manufacturing strategy is described in detail for the hybrid approach. This is followed by a comprehensive analysis of the substrate as well as the powdery filler material including destructive as well as nondestructive testing methods. Essential aspects like the sphericity of the powder, its surface condition, as well as the particle size distribution, and its density were addressed. The processing is described comprehensively addressing process development steps and the used process parameters.

The postprocessing is also described addressing hot isostatic pressing (HIP) and the applied three-stage heat treatment. The hot tensile testing and the

wide-ranging analysis comprising microscopic examination of the fracture surfaces, voluminous radiographic examination of the porosity including size and distribution as well as the determination of the grain size, and the orientation *via* electron backscattered diffraction were performed to interlink the mechanical properties with the processing-related microstructure.

Based on the fundamental results, the manufacturing of more complex demonstrator parts was addressed. This includes the selection of a typical application, the transfer of the strategy, as well as the proof of concept.

V. CONCLUSIONS

The difficulties associated with the Additive Manufacturing of superalloys prone to hot cracking are widely known. However, it was demonstrated that the processing of Mar-M-247 and CM 247 LC is feasible *via* tailored hybrid manufacturing. The present approach interlinks material-scientific aspects with state-of-the-art manufacturing engineering. Hence, it can be concluded that this procedure works for the aforementioned alloys, but is not limited to them.

The comprehensive analysis of the filler material leads to the conclusion that the production routes for these multielemental alloy powders are under control which will certainly improve the availability of these high-performance materials in the field of Additive Manufacturing.

The results from the process development indicate the high potential of the hybrid approach especially in the context of tailored Additive Manufacturing system technology. This becomes obvious when considering that the Lasertec 65 3D allows to change between Laser Metal Deposition with powder (additive) and high-end milling processing (subtractive) in one and the same setting. Moreover, the applied inductors can easily be individualized *via* Additive Manufacturing itself.

The mechanical characterization of the samples showed superior mechanical properties for the hybrid-manufactured samples. Here, all specimens showed the typical characteristics of nickel-based superalloys featured by a continuous transition from elastic-to-plastic deformation without any discontinuity within the graphs. Nevertheless, wide-ranging investigations regarding the grain size, γ' precipitates, and crystallographic structure based on a higher number of samples for a statistical coverage are currently in process.

It was proven that the carbides as well as the γ' precipitates show distinct differences in the size and morphology when comparing the hybrid samples and the ingot. This, presumably, is the reason for the higher tensile strength, the superior elongation at fracture, and the clearly more uniform fracture surfaces. Nevertheless, the absolute values will be questioned and reflected in the next step.

X-ray computer tomography investigations show that the AM samples had noticeable higher microporosity. The latter is caused by the process-specific carrier and

shielding gas but seemed to have no major impact on the achieved mechanical values. Moreover, the mechanical properties of the ingot samples are significantly lower although they were manufactured under vacuum.

The hybrid AM samples have significantly smaller grain sizes and fine carbides homogeneously distributed at the grain boundaries. The latter can help to avoid grain boundary sliding and dislocation movements. In addition to this, the coherent γ' precipitates are uniform and homogeneously distributed.

REFERENCES

1. R. Reed: *The Superalloys Fundamentals and Applications*, Cambridge University Press, Cambridge, 2006.
2. M.M. Coporation: Nickel Base Alloy. USA Patent 3720509, 14 Dezember 1970.
3. Al. Gunderson, S.J. Setlak, and W.F. Brown: *Aerospace Structural Metals Handbook*, vol. 6, CINDAS LLC, West Lafayette, Indiana, 2007 (Revised).
4. C. Yan, L. Zhengdong, A. Godfrey, L. Wei, and W. Yuding: *Mater. Sci. Eng. A*, 2014, vol. 30 (2), pp. 153–64.
5. C.H. Tsai and W. Weite: *Metall. Mater. Trans. A*, 1999, vol. 30A (2), pp. 417–26.
6. A. Hübner: *Untersuchungen über den Einfluss und die Wirkungen von Stickstoffzusätzen im Schutzgas auf das Heißbrissverhalten ausgewählter heißbrissempfindlicher Nickel-Basiswerkstoffe*, Magdeburg, Otto-von-Guericke-Universität Magdeburg (Diss.), 2005.
7. U. Dilthey: *Schweißtechnische Fertigungsverfahren 2 - Verhalten der Werkstoffe beim Schweißen*, Springer, Aachen, 2005, vol. 3.
8. W. Liu, X. Tian, and X. Zhang: *Weld. J. (Weld. Res. Suppl.)*, 1996, pp. 297–304.
9. X. Cao, B. Rivaux, M. Jahazi, J. Cuddy, and A. Birur: *J. Mater. Sci.*, 2009, vol. 44, pp. 4557–71.
10. E.M. Lehouckey, G. Palumbo, and P. Lin: *Metall. Mater. Trans. A*, 1998, vol. 29A (12), pp. 3069–79.
11. G. Göbel: *Erweiterung der Prozessgrenzen beim Laserstrahlschweißen heißbrissgefährdeter Werkstoffe*. Dresden & Stuttgart, Technische Universität Dresden (Diss.), 2008.
12. F. Brückner: *Modellrechnungen zum Einfluss der Prozessführung beim induktiv unterstützten Laser-Pulver-Auftragschweißen auf die Entstehung von thermischen Spannungen, Rissen und Verzug*. Dresden, Technische Universität Dresden (Diss.), 2011.
13. A. Seidel: *Heißbrissreduzierung durch magnetofluidynamische Maßnahmen beim Laserauftragschweißen am Beispiel der Nickelbasis-Superlegierung Mar-M-247*. Thesis, Dresden, Technische Universität Dresden, 2014 (pursuing <http://gepris.dfg.de/gepris/projekt/396298896>).
14. K. Gupta, N.K. Jain, and R.F. Laubscher: *Hybrid Machining Processes: Perspectives on Machining and Finishing*, Springer International Publishing AG, 2016.
15. W. Grzesik: *Advanced Machining Processes of Metallic Materials: Theory, Modelling, and Applications*, Elsevier, San Diego, 2016, vol. 2.
16. E. Beyer: *Schweißen mit Laser - Grundlagen*, Springer, Berlin, 1995.
17. D. Lepski and F. Brückner: *Laser Cladding. The Theory of Laser Materials Processing—Heat and Mass Transfer in Modern Technology*, Springer, Dresden, 2009, pp. 235–79.
18. C.S. Wu: *Welding Thermal Processes and Weld Pool Behaviors*, CRC Press, London, 2010.
19. D.M. Stefanescu: *Science and Engineering of Casting Solidification*, 2nd ed., Springer Science+Business Media, LLC, Columbus, Ohio, USA, 2009.
20. S. Kou: *Welding Metallurgy*, Wiley Interscience, Wisconsin, 2003.
21. W. Kurz, and D. Fisher: *Fundamentals of Solidification*, Fourth Revised Edition, Lausanne, Trans Tech Publications Ltd, 2005 (Reprinted).
22. R. Bürgel, Hans.J. Maier, and T. Niendorf: *Handbuch Hochtemperatur-Werkstoffe Grundlagen, Werkstoffbeanspruchungen, Hochtemperaturlegierungen und -beschichtungen.*, Vieweg + Teubner Verlag, Wiesbaden, 2011, vol. 4.
23. T.M. Pollock, W.H. Murphy, E.H. Goldman, D.L. Uram, and J.S. Tu: *Superalloys 1992*, Proc. 7th Int. Symp. on Superalloys, Seven Springs/Pa., The Minerals, Metals & Materials Society, Warrendale/Pa., 1992, pp. 125–34.
24. M.A. Taha and W. Kurz: About Microsegregation of Nickel Base Superalloys *Zeitschrift für Metallkunde*, 1981, vol. 72, pp. 546–49.
25. D. Ma and P.R. Sahm: Einkristallerstarrung der Ni-Basis-Superlegierung SRR99, Teil2: Mikroseigerungsverhalten der Legierungselemente *Zeitschrift für Metallkunde*, 1996, vol. 87, pp. 634–39.
26. M.S.A. Karunaratne, D.C. Cox, P. Porter, and R.C. Reed, *Superalloys 2000*, Proc. 9th Int. Symp. on Superalloys, Seven Springs/Pa., The Minerals, Metals & Materials Society, Warrendale/Pa., 2000, pp. 263–72.
27. A.R.E. Singer and P.H. Jennings: *J. Inst. Met.*, 1947, vol. 74, pp. 197–212.
28. H.F. Bishop, C.E. Ackerland, and S.W. Pellini: *Trans. Am. Foundry Soc.*, 1952, vol. 60, pp. 818–913.
29. W.S. Pellini: *Foundry*, 1952, vol. 80, pp. 125–99.
30. C. Borland: *Br. W. J.*, 1960, vol. 7, pp. 508–12.
31. M. Rappaz, J.M. Drezet, and M. Gremaud: *Metall. Mater. Trans. A*, 1999, vol. 30A, pp. 449–55.
32. S. Bonns, M. Seifert, J. Hannweber, U. Karsunke, S. Kühn, D. Pögen, and E. Beyer: *Invited Paper at the 9th International Conference on Photonic Technologies LANE 2016*, Physics Procedia, vol. 83, pp. 1–1450.
33. K.-T. Hsu, H.-S. Wang, W.-B. He, C.-M. Kuo, H.-Y. Bor, and C.-N. Wei: *Suppl. Proc. Mater. Properties, Charact. Model.*, 2012, vol. 2, pp. 667–72.
34. DIN EN ISO 6892-2:2011-05, Metallic materials—Tensile testing—Part 2: method of test at elevated temperature (ISO 6892-2:2011).
35. M.V. Nathal and R.A. Mackay: *Acta Metallurgica et Materialia*, 1991, vol. 39, pp. 2771–81.
36. R. Baldan, C.A. Nunes, M.J.R. Barboza, A.M.S. Costa, R. Bogado, and G.C. Coelho: *Int. Conf. Adv. Mater.*, 2009, vol. 11, pp. 56–67.
37. J. Davids: *Heat-Resistant Materials*, The Materials Information Society, Materials Park, Ohio, 1997.
38. A. Basak and S. Das: *J. Alloys Compd.*, 2017, vol. 705, pp. 806–16.
39. X. Wang, N. Luke, B. Pang, M.M. Attallah, and M.H. Loretto: *Acta Materialia*, 2017, vol. 128, pp. 87–95.
40. J.R. Kattschuk: *MAR-M247, Aerospace Structural Metals Handbook*, 1999, pp. 1–7.
41. P. Heuler and H. Huff: *Niedrigschwingspielzahl-Ermüdung (LCF) von Turbinenrädern aus Nickelbasis-Gußwerkstoffen Teil II: Untersuchungen an dem Werkstoff MAR-M247 LC FK HIP*, Final report for the FVV-project Nr. 438, Industrieanlagen-Betriebsgesellschaft mbH (IABG), Fraunhofer-Institut für Betriebsfestigkeit (LBF), Darmstadt, 1994.
42. D. Gelmedin and K.H. Lang: *Ermüdungsverhalten von Hochtemperaturwerkstoffen bei hohen Grundlasten*, Final report for the FVV-project Nr. 867, Institut für Werkstoffkunde I, Universität Karlsruhe, 2010.
43. M. Prager and C.S. Shira: *Weld Res. Council Bull.*, 1968, vol. 6, pp. 128–155.
44. J.M. Kalinowski: *Weldability of a Nickel-Based Superalloy*, NASA Contractor Report 195376, August 1994.
45. G. Cam and M. Kocak: *Int. Mater. Rev.*, 2013, vol. 43, pp. 1–44.
46. A. Basak and S. Das: *JOM*, 2018, vol. 70, pp. 53–59.